Ultrastrong medium-entropy single-phase alloys designed via severe lattice distortion

Sohn, Seok Su; Kwiatkowski da Silva, Alisson; Ikeda, Yuji; Körmann, Fritz; Lu, Wenjun; Choi, Won Seok; Gault, Baptiste; Ponge, Dirk; Neugebauer, Jörg; Raabe, Dierk

DOI
10.1002/adma.201807142

Publication date
2019

Document Version
Accepted author manuscript

Published in
Advanced Materials

Citation (APA)
Sohn, S. S., Kwiatkowski da Silva, A., Ikeda, Y., Körmann, F., Lu, W., Choi, W. S., Gault, B., Ponge, D., Neugebauer, J., & Raabe, D. (2019). Ultrastrong medium-entropy single-phase alloys designed via severe lattice distortion. *Advanced Materials*, *31*(8), Article 1807142. https://doi.org/10.1002/adma.201807142

Supporting Information

Ultrastrong medium-entropy single-phase alloys designed via severe lattice distortion

Seok Su Sohn, Alisson Kwiatkowski da Silva, Yuji Ikeda, Fritz Körmann, Wenjun Lu, Won Seok Choi, Baptiste Gault, Dirk Ponge, Jörg Neugebauer, and Dierk Raabe*

Experimental Section

Ab initio calculations: The *ab initio* calculations have been performed within the framework of density functional theory (DFT) employing the VASP code[S1,S2] and the projector-augmented wave method.[S3] The exchange-correlation energy has been treated within the generalized gradient approximation.[S4] A plane wave cutoff energy of 300 eV was chosen throughout all calculations. The chemical disorder was simulated by special quasi-random structures (SQS).[S5] The SQS contains 108 atoms and have been constructed[S6] by minimizing the correlation functions of the first two nearest-neighbor shells. The equilibrium volume has been determined by computing total energies for eleven volumes around the equilibrium volume for one SQS in combination with the six inequivalent permutations. The internal atomic coordinates of each supercell were fully optimized with energy convergence criteria set to be less than 10^{-4} eV per atom. To avoid artificial cell shape relaxations due to limited super cell size, the cubic cell shape has been kept fixed. The Methfessel-Paxton technique[S7] with a smearing value of 0.1 eV has been used. The individual equilibrium volumes of each considered supercell vary less than 0.03% around the averaged theoretical equilibrium volume of 3.575 Å. To derive the mean square atomic displacement (MSAD) we considered four different SQS and for each of them all six permutations of internal species (VCoNi, VNiCo, CoVNi,...) have been investigated *i.e.*, in total twenty-four distinct supercells were considered. The averaged MSAD value is then derived as follows.[39,40] First the elemental MSAD values are computed as Equation (3):

$$\mathrm{MSAD}_A = \frac{1}{|S^A|}\sum_{I\in S^A}(R_I - R_I^{\mathrm{ideal}})^2 \qquad (3)$$

where A denotes the constituent element, S^A is the set of the indices for the sites occupied by A, R_I is the relaxed position at site I, and R_I^{ideal} is the corresponding position on the ideal lattice. The averaged MSAD value is obtained by averaging over the MSAD_A values. For a comprehensive overview on *ab initio* calculations for HEAs we refer to ref. S8.

Alloy fabrication: The VCoNi alloy was synthesized via melting and casting in a vacuum induction equipment (model; MC100V, Indutherm, Walzbachtal-Wossingen, Germany) using pure metals (the purity of each raw material was 99.9% at least). The master alloy of 150 g was molten and poured into rectangular graphite molds of 100 × 35 × 8 mm^3 size. The cast blocks were homogenized at 1,200 °C for 24 h in evacuated quartz ampules, pickled in a 20% HCl solution, and cold-rolled to the thickness reduction of 75%. The rolled sheets of 1.5 mm thick were then recrystallized at temperatures between 900 and 1,200 °C for 1 min or 1 h in an Ar atmosphere, followed by water-quenching. The bulk chemical compositions of all the studied alloy were confirmed by wet-chemical analysis. The CrCoNi alloy was also fabricated and cold-rolled with the same procedure and then recrystallized at 900 °C for 1 h to compare mechanical properties with that of the VCoNi alloy.

Microstructural characterization: The microstructures of the alloys were analyzed using multiple techniques. The crystal structure and lattice parameter of the alloy were identified by X-ray diffraction (Cu $K_{\alpha 1}$ radiation, scan rate: 2 deg per min, scan step size: 0.02 deg). EBSD measurements were performed using a field emission scanning electron microscope (FE-SEM, JEOL, JSM-6500F, USA). EBSD specimens were prepared by mechanical polishing using a colloidal silica suspension. The average misorientation of a given point relative to its neighbors is calculated using the kernel average misorientation (KAM) approach. The KAM was calculated up to the third neighbor shell with a maximum misorientation angle of 5°. The KAM map reveals the deformation-induced local orientation gradients. ECCI analyses were carried out using a Zeiss-Merlin instrument (Zeiss Crossbeam 1,540 EsB, Zeiss, Oberkochen, Germany).

Chemical uniformity of the alloys was investigated using energy-dispersive X-ray spectroscopy (EDS) (Inca Energy 350, Oxford Instruments, Abingdon, United Kingdom) at the microscopic scale, and APT (LEAP 5,000XS, Cameca Instruments Inc., Madison, WI, USA) at the atomic scale. APT specimens were produced using a focused ion beam (FIB, Helios

NanoLab 600i, FEI, Hillsboro, USA) from regions including grain boundaries revealed by a preceding EBSD scan. APT measurements were performed with approx. 80% detection efficiency at a base specimen temperature of 60 K in laser-pulsing mode at a wavelength of 355 nm, 30 pJ pulse energy and 500 kHz pulse repetition rate. APT data reconstruction and analysis were carried out using the commercial software IVAS® by Cameca using the protocol introduced by Geiser et al.[S9] and detailed in Gault et al.[S10] The atomic scale chemical uniformity was investigated using radial distribution function (RDF) analysis from APT data. The RDF analysis represents the radial concentration profile starting from each and every detected atom, thus the probability to find a neighboring atom *j* at distance *r* when a reference center atom is *i*.[S11,S12] Here, V was taken as the center ion with 0.1 nm of bin width and 1.5 nm of maximum distance (*r*). The measured concentration at each position was normalized with respect to the average bulk concentration. Scanning transmission electron microscopy (STEM) imaging and STEM-EDS were conducted in an aberration-corrected STEM/TEM (FEI Titan Themis) at 300 kV. For high resolution imaging a probe semi-convergence angle of 17 mrad and an inner and outer semi-collection angle of 73-350 mrad were used. TEM foils were prepared by FIB lift-out technique.

Mechanical tests: Flat specimens for tensile testing were sectioned from the recrystallized alloy by electrical discharge machining. The gauge length, width, and thickness of the tensile specimens were 6.4, 2.5, and 1.5 mm, respectively. Uniaxial tensile tests were carried out at room temperature using a universal testing machine (model: 8801, Instron, Canton, MA, USA) at a crosshead speed of 6.4×10^{-3} mm s^{-1}. The strain during the tensile test was measured by digital image correlation using the Aramis system (ARAMIS 5M, GOM optical measuring techniques, Germany). The representative data were obtained by averaging three values at each datum point and are reported with the s.d. The deformation mechanisms were investigated by EBSD and ECCI at several strain levels. All of the sample regions analyzed by ECCI were first measured by EBSD to obtain the specific orientation information corresponding to each region.

Elastic constant measurements: The density of the alloy was first measured to be 7.74 g cm^{-3} using a Mettler-Toledo XP205 device (Mettler-Toledo AG, Switzerland) for the VCoNi alloy annealed at 900 °C for 1h. Shear modulus (G) and Young's modulus (E) were measured using an ultrasonic pulse-echo measuring system (HKLAB CO., HKL-01-UEMT) at room temperature. The specimen of 20 × 20 × 1.5 mm^3 was polished mechanically and then tested five times. The poisson's ratio (ν) was calculated using an elastic equation for isotropic bodies[S13] and the measured shear and Young's moduli. The measured G, E, and ν were 192 GPa, 72 GPa, and 0.334, respectively.

Estimation of strengthening by various mechanisms: The yield strength, i.e. the flow resistance measured at the onset of plastic deformation is obtained as a summation of the five individual yield strength contributions in polycrystalline materials: 1) intrinsic friction stress (which is the main objective in the current study); 2) grain-boundary strengthening (the so-called Hall-Petch effect); 3) dislocation hardening (creating long-range stress fields scaling with ~1/r); 4) precipitation hardening; and 5) oxide dispersion hardening. Regarding the dislocation content, the fully-recrystallized materials used in our study have generally very low dislocation density values of the order of 10^{11}-10^{12} m^{-2}.[S14,S15] According to the Bailey–Hirsch formula,[S16] the contribution of dislocation hardening for the VCoNi alloy annealed at 900 °C for 1h is described as:

$$\Delta\sigma_{dis} = M\alpha Gb\rho^{1/2} \quad (4)$$

where α = 0.2 is a constant for fcc materials, G = 72 GPa is the shear modulus, ρ is the dislocation density, and b = $2^{1/2}$ $a_{fcc}/2$ = 0.255 nm is the magnitude of the Burgers vector. The lattice parameter a_{fcc} = 0.3601 nm. Thus the contribution of dislocation hardening amounts to only 3~11 MPa. We showed that there are no precipitates in our VCoNi alloy. For the oxides, owing to their large particle size, a model for particulate-reinforced metal matrix composite was employed to calculate the associated strengthening effect. Equation (4) incorporates the Orowan

strengthening effect and the modified shear lag model ascribing the entire strengthening effect to the load bearing feature of the hard reinforcement:[S17,S18]

$$\sigma_y = \sigma_y'(1 + 0.5f)(1 + \frac{\Delta\sigma_{Orowan}}{\sigma_y'}) \qquad (5)$$

where σ'_y is the reduced yield strength, arising from lattice friction and grain boundary strengthening of the fcc matrix, f is the volume fraction of the particles, and $\Delta\sigma_{Orowan}$ is the strengthening contribution from the Orowan mechanism. The Orowan strengthening can be calculated by the Ashby-Orowan equation:[S19]

$$\Delta\sigma_{Orowan} = \left(0.538 \cdot \frac{Gbf^{0.5}}{D}\right) \ln(\frac{D}{2b}) \qquad (6)$$

where f = 0.31 ± 0.11% is the volume fraction of particles, and D is the real spatial diameter of the particles. The latter value can be calculated from the average diameter of the precipitates (D_0=0.95 ± 0.32 μm) measured from the intersection plane based on the equation of $D = (3/2)^{1/2}D_0$. The measured yield strength (σ_y) is 767 MPa for the VCoNi alloy annealed at 900 °C for 1hr. According to equations (5) and (6), $\Delta\sigma_{Orowan}$ is evaluated to be 3 MPa. From this value, σ'_y is determined to be 763 MPa. These three contributions (dislocation, precipitation, and oxide) to the yield strength in the current alloys are all negligible (6-14 MPa) compared to the much larger contribution of the measured lattice friction stress obtained after Hall-Petch correction. This analysis thus reveals that the corrected yield strength, hence, can indeed serve serving as an excellent a good measure of the lattice distortions acting in the alloy. This means that we can evaluate the friction stress by subtracting only the grain-boundary strengthening contribution from the measured yield strength. Based on this conclusion, we compared the friction stress of the VCoNi alloy with those observed for the CrCoNi MEA, CrMnFeCoNi HEA, and conventional austenitic steels in Table S2.

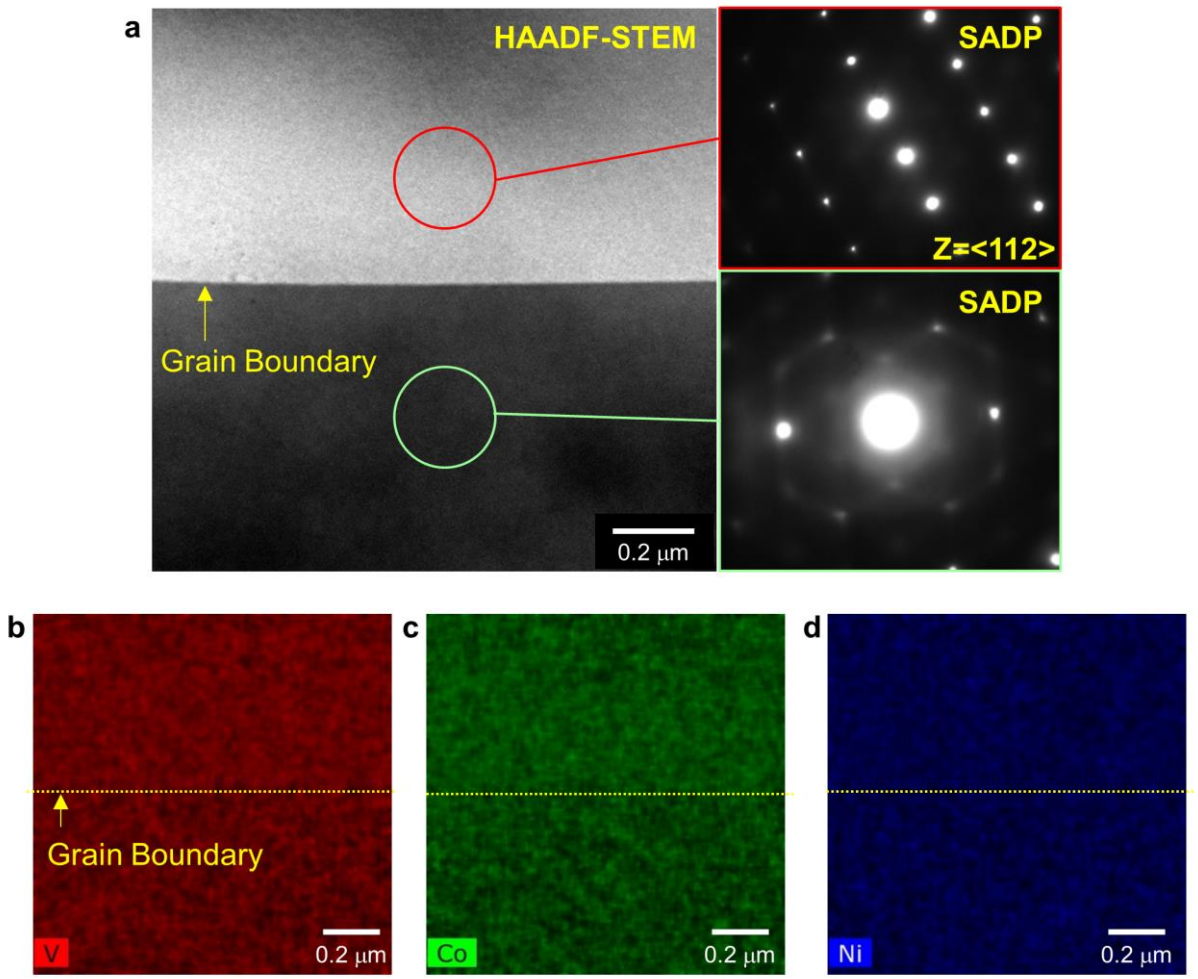

Figure S1. Chemical homogeneity analysis at nano-scale by high angle annular dark-field scanning TEM (HAADF-STEM) analysis. a) HAADF-STEM micrograph and selected-area diffraction (SAD) patterns suggest that no precipitates or ordered phase occur at the grain boundaries. b-d) STEM-EDS maps of V, Co, and Ni shows there is no substantial chemical segregation of V, Co or Ni at the grain boundaries.

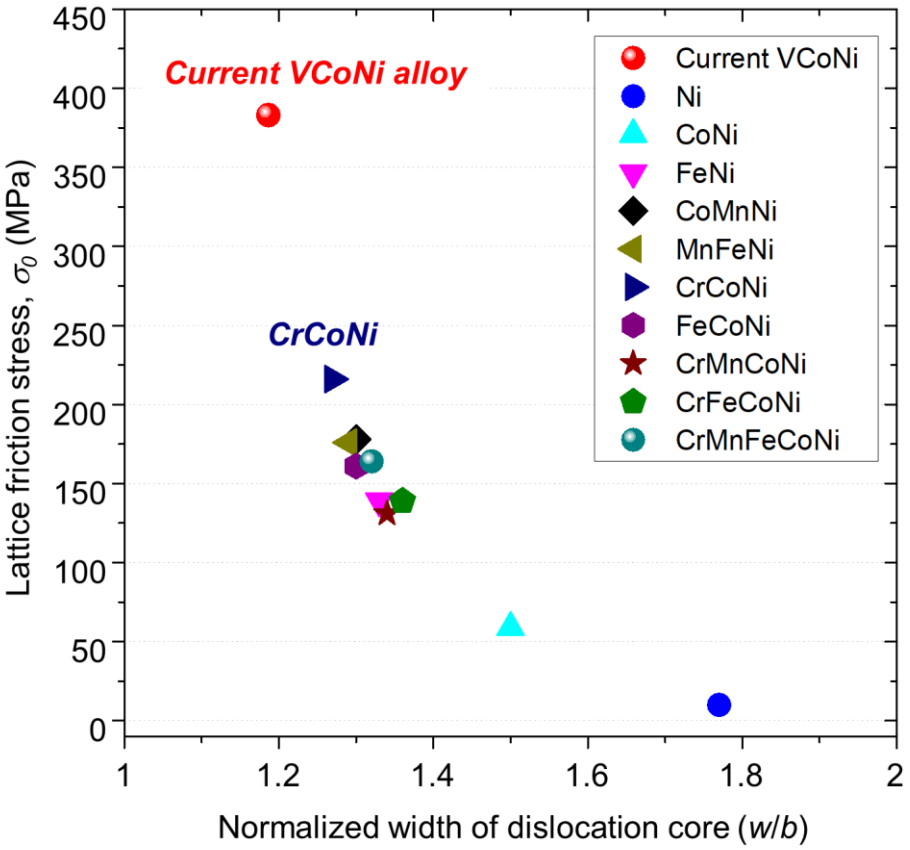

Figure S2. Friction stress (σ_0) and the normalized dislocation width (w/b, width/Burgers vector) of the fcc equiatomic alloys.[21,28,29] The alloys showing higher friction stress have much lower w/b values, implying more difficult dislocation glide in them. The detailed values are summarized in Table S3.

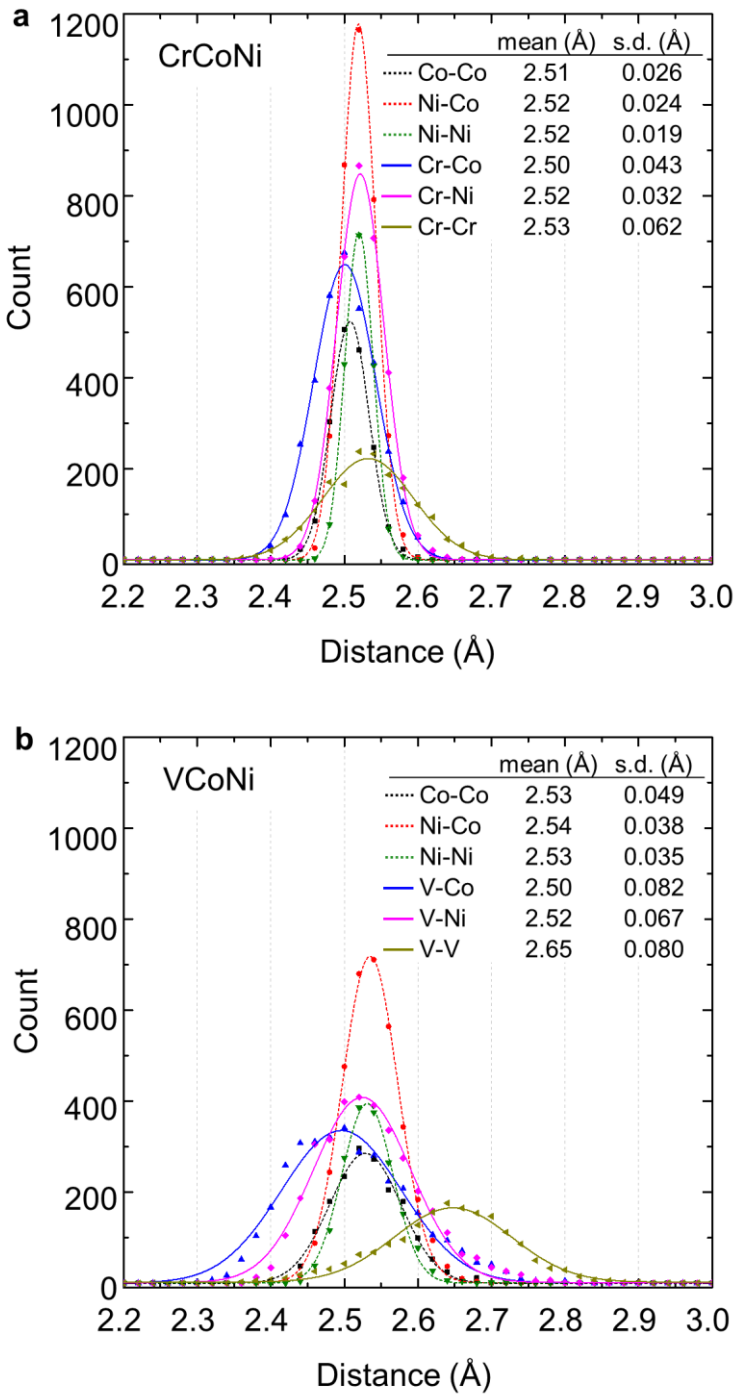

Figure S3. *Ab initio* calculations for the local lattice distortion effect. a) First nearest-neighbor distances of each elemental pairs in the CrCoNi. b) First nearest-neighbor distances of each elemental pairs in the VCoNi. The computed bond distances were fitted to normal distribution functions to evaluate the mean value and their fluctuations. The mean and s.d. indicate the average distance and standard deviation, respectively.

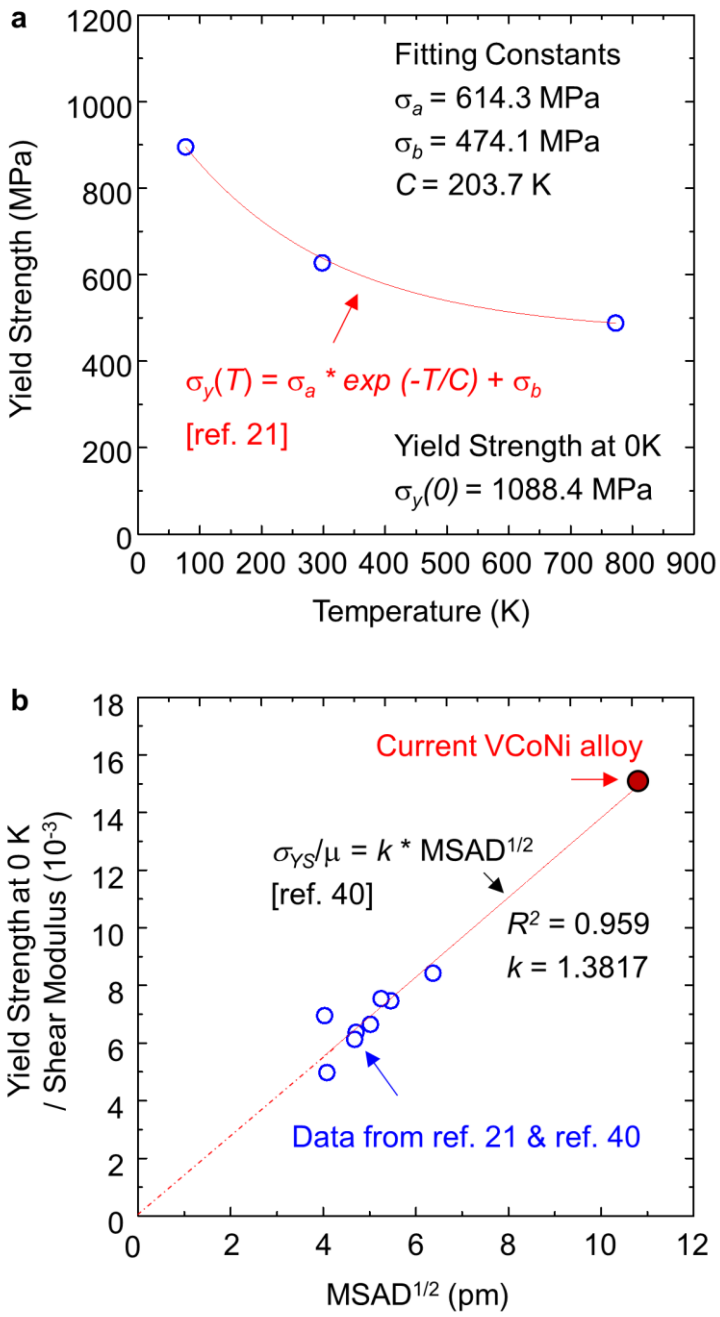

Figure S4. Linear correlation between the MSAD values and the yield strength. a) Yield strength at 77 K, 298 K, and 773 K for the VCoNi alloy annealed at 950°C for 1h (grain size of 18.7 μm). The data are fitted by the equation where σ_a, σ_b, and C are fitting constants. The calculated yield strength at 0 K is 1088.4 MPa. b) Yield strength at 0K normalized by shear modulus and the square root of the MSAD value for the equiatomic alloys.[21,40] The current alloy also scales linearly well with the given equation. By adding our data, the linear correlation shows an even better fitting with R^2 of 0.959 than the previous result (R^2 of 0.801).[40]

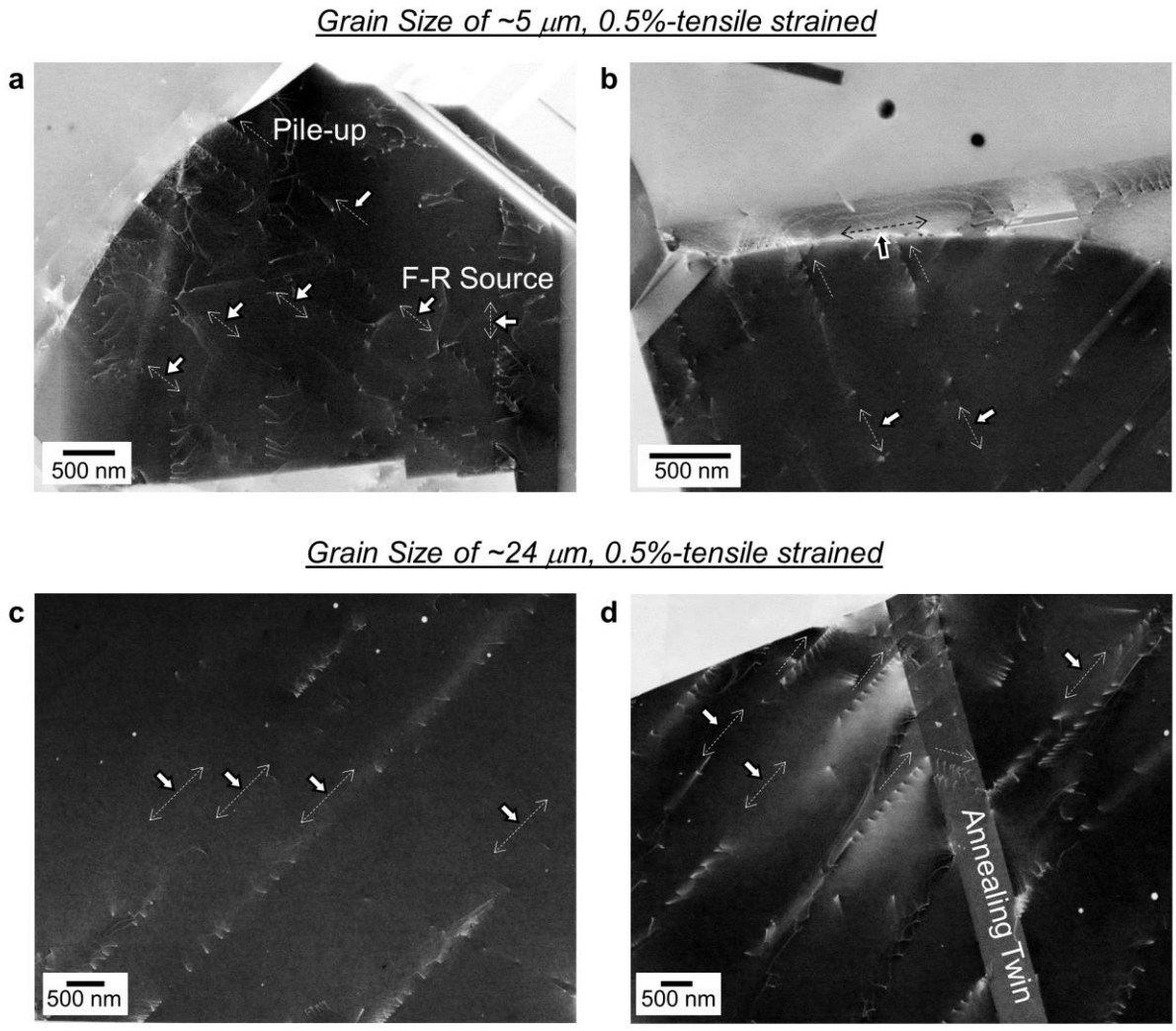

Figure S5. Dislocation source observation by electron channeling contrast imaging (ECCI) analyses of the 5 μm-and 24 μm-sized grain at 0.5% tensile strain. a) Dislocations are nucleated inside a grain as a Frank-Read source type and piled-up at grain boundaries. b) Frank-Read sources are activated and piled-up at a grain boundary (white arrow). Additional Frank-Read source is activated in nearest-neighbor grain (black arrow) not at grain boundary, but inside grain. c) Dislocations are nucleated inside a grain in coarse grain. d) Frank-read sources are activated and gliding dislocations are transferred across annealing twin boundary relatively easily considering a spacing of dislocations at the twin boundary (white box).

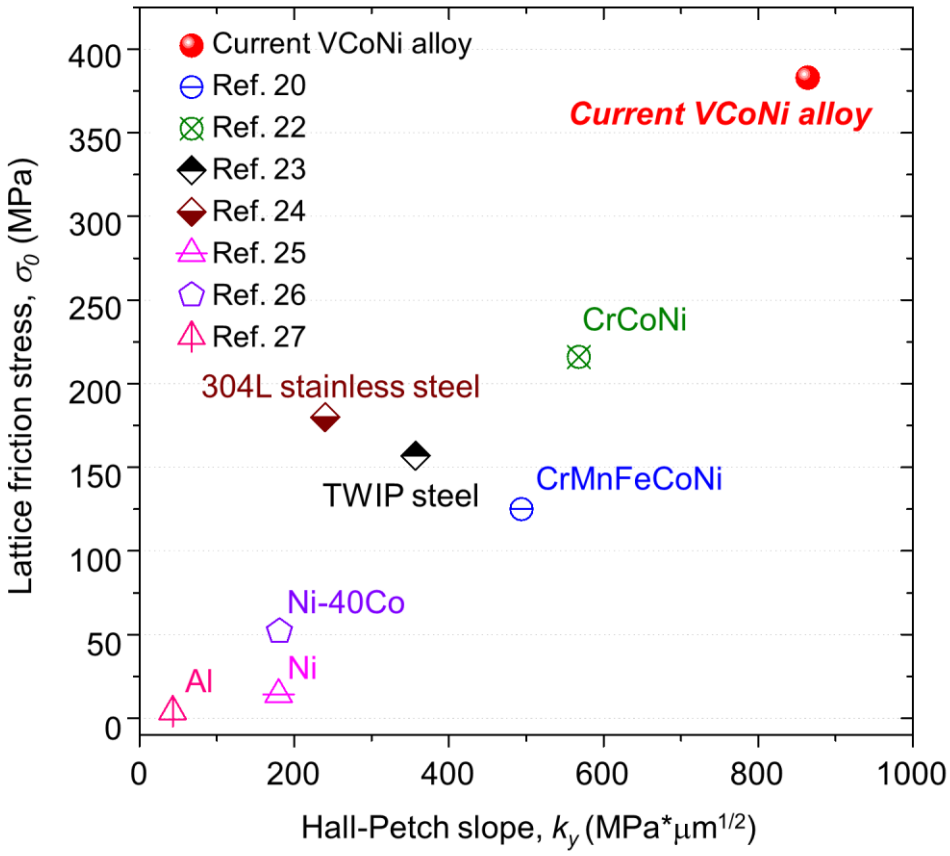

Figure S6. Frictional stress (σ_0) and Hall-Petch coefficient (k_y) of VCoNi alloy, previous medium- or high-entropy alloys and conventional austenitic steels.[20,22-27] The coefficients of the Hall-Petch relation have proportional tendency to the frictional stress although the tendency slightly deviates in conventional structural steels. Note that the coefficient and frictional stress are typically higher, in particular for high- or medium-entropy alloys.

Table S1. Room temperature tensile properties and average grain sizes of the VCoNi and CrCoNi alloys according to various annealing conditions.

Alloy	Annealing condition	Average grain size (μm)	YS (MPa)	UTS (MPa)	El. (%)
VCoNi	900°C for 1min	2.0 ± 1.5	991 ± 8	1359 ± 2.1	38 ± 0.5
	900°C for 1h	5.6 ± 3.1	767 ± 5	1221 ± 0.5	46 ± 0.1
	950°C for 1h	18.7 ± 13.9	602 ± 7	1123 ± 8.0	51 ± 1.6
	1000°C for 1h	27.8 ± 19.5	517 ± 8	1049 ± 0.5	55 ± 1.5
	1200°C for 1h	122.2 ± 76.4	461 ± 6	886 ± 4.0	58 ± 0.1
CrCoNi	900°C for 1h	11.0 ± 6.7	389 ± 6	883 ± 5.0	68 ± 1.2

Table S2. Frictional stress (σ_0) and Hall-Petch coefficient (k_y) of VCoNi alloy, previous medium- or high-entropy alloys and conventional austenitic steels.

Alloy	Slope, k_y (MPa*μm$^{1/2}$)	σ_0 (MPa)	Comment
VCoNi	864	383	Current alloy
CrCoNi	568	216	Ref. 22
CrMnFeCoNi	494	125	Ref. 20
Fe-22Mn-0.6C (wt%) TWIP steel	357	157	Ref. 23
304L stainless steel	240	180	Ref. 24
Pure Ni	180	14.2	Ref. 25
Ni-40Co	181	51.9	Ref. 26
Pure Al	43	4	Ref. 27

Table S3. Shear modulus (G), Poisson's ratio (ν), frictional stress (σ_0), and the normalized dislocation width (w/b, width/Burgers vector) of the fcc equiatomic alloys.

Alloy	G (GPa)	ν	σ_0 (MPa)	w/b	Comment
VCoNi	72	0.33	383	1.19	Current alloy
Ni	76	0.31	10	1.77	Ref. 21,28
NiCo	84	0.29	59	1.5	Ref. 21,28
NiFe	62	0.34	139	1.33	Ref. 21,28
NiCoMn	77	0.23	178	1.3	Ref. 21,28
NiFeMn	73	0.24	176	1.29	Ref. 21,28
NiCoCr	87	0.3	216	1.27	Ref. 21,28
NiCoFe	60	0.35	161	1.3	Ref. 21,28
NiCoCrMn	77	0.22	131	1.34	Ref. 21,28
NiCoFeCr	84	0.28	139	1.36	Ref. 28, 29
NiCoCrFeMn	80	0.26	164	1.32	Ref. 21,28

References

[S1] G. Kresse, J. Furthmüller, *J. Comp. Mater. Sci.* **1996**, *6*, 15.

[S2] G. Kresse, J. Furthmüller, *Phys. Rev. B* **1996**, *54*, 11169.

[S3] P. E. Blöchl, *Phys. Rev. B* **1994**, *50*, 17953.

[S4] J. P. Perdew, K. Burke, M. Ernzerhof, *Phys. Rev. Lett.* **1996**, *77*, 3865.

[S5] A. Zunger, S. Wei, L. G. Ferreira, J. E. Bernard, *Phys. Rev. Lett.* **1990**, *65*, 353.

[S6] The special quasi random structures have been generated with the spcm program. For further information please contact Prof. Andrei V. Ruban (a.v.ruban@gmail.com).

[S7] Methfessel, M. & Paxton, A. T. High-precision sampling for Brillouin-zone integration in metals. *Phys. Rev. B* **1989**, *40*, 3616.

[S8] Y. Ikeda, B. Grabowski, F. Körmann, *Mater. Charact.*, DOI: 10.1016/j.matchar.2018.06.019.

[S9] B. P. Geiser, D. J. Larson, E. Oltman, S. Gerstl, D. Reinhard, T. F. Kelly, T. J. Prosa, *Microsc. Microanal.* **2009**, *15*, 292.

[S10] B. Gault, D. Haley, F. de Geuser, M. P. Moody, E. A. Marquis, D. J. Larson, B. P. Geiser, *Ultramicroscopy* **2011**, *111*, 448.

[S11] M. K. Miller, E. A. Kenik, *Microsc. Microanal.* **2004**, *10*, 336.

[S12] F. De Geuser, W. Lefebvre, D. Blavette, *Philos. Mag. Lett.* **2006**, *86*, 227.

[S13] L. Vitos, *Computational Quantum Mechanics for Materials Engineers*, Springer-Verlag, London, UK **2007**.

[S14] I. Baker, F. Meng, M. Wu, A. Brandenberg, *J. Alloys Compd.* **2016**, *656*, 458.

[S15] D. Wu, J. S. C. Jang, T. G. Nieh, *Intermetallics*, **2016**, *68*, 118.

[S16] T. H. Courtney, *Mechanical Behavior of Materials*, Waveland, Illinois, USA **2005**.

[S17] N. Ramakrishnan, *Acta Mater.* **1996**, *44*, 69.

[S18] Z. Zhang, D. L. Chen, *Scr. Mater.* **2006**, *54*, 1321.

[S19] T. Gladman, *Mater. Sci. Technol.* **1999**, *15*, 30.